Spatially Resolved Fast-Time Vibrometry Using Ultrawideband FMCW Radar Systems

Lukas Piotrowsky, *Graduate Student Member, IEEE*, and Nils Pohl, *Senior Member, IEEE*

Abstract—**Highly accurate vibrometry and ranging are important topics in the industrialized economy. Wherever optical measurement technology fails due to its high prices and vulnerability within harsh environments, millimeter-wave (mmWave) radar technology is well suited. This article introduces a signal processing chain for ultrawideband frequency-modulated continuous-wave (FMCW) radar. It uses fast-time measurement to evaluate the instantaneous phase, thus allowing for spatially resolved sensing of multiple simultaneously vibrating radar targets, faster than the chirp rate. In order to accomplish this, a sophisticated error model and a calibration scheme were derived. We used three FMCW radar systems covering a broad range of the mmWave spectrum to demonstrate the signal processing approach. In contrast to the commonly used slow-time measurement principle, the highest detectable frequency was improved from 55 Hz to at least 16 kHz, which is the upper limit of the audio range. Up to 10 kHz could be measured with an underlying large-scale motion of 0.4 m/s, while the vibration displacement was at a minimum of 30 nm.**

Index Terms—**Displacement measurement, distance measurement, estimation error, millimeter-wave (mmWave) radar, processing algorithms, radar measurements, radar theory, ultrawideband radar, vibration measurement, vibrometers.**

I. INTRODUCTION

WITHIN the last few years, millimeter-wave (mmWave) frequency-modulated continuous-wave (FMCW) radar systems have been widely used for short-range measurements. Due to their low peak power and their simple homodyne structure, they allow for low-cost chip integration with high bandwidth and, hence, with the highest range resolution. Current research deals with ranging, synthetic aperture radar (SAR) imaging, material characterization, and biomedical applications. Nowadays, well-known commercial applications for mmWave sensor technology are autonomous driving, ultrafast communication (5G), tank-level probing, or safety sensory. Here, mmWave sensory is outstanding due to its advantageous properties, which enables sensing even within the harshest environments.
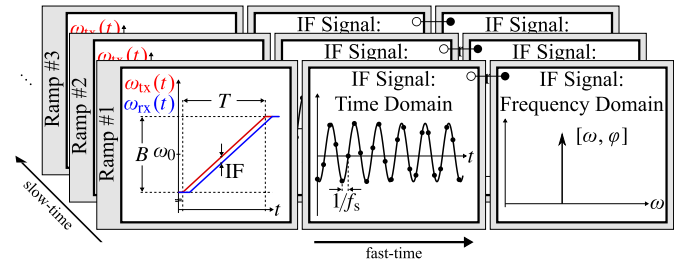
Fig. 1.   Illustration of the slow- and fast-time measurement principle using FMCW radar systems.

Many applications require highly sensitive measuring of mechanical vibrations. A common example is wear indication, and fault detection of rotating machines [1]–[4] or structures [5]–[10], e.g., bridges or high-rise buildings. Furthermore, vibrometry deals with health monitoring to measure the heartbeat as well as the respiration rate [11]–[15] or extracting speech by vocal vibrations [16]–[19]. Typically, highly accurate instruments for measurement of vibrations and distances are contact-based [20] or use fragile laser devices.

In this article, we demonstrate a spatially resolved method for highly precise vibration measurement of radar targets in motion using ultrawideband FMCW radar systems. In contrast to common vibrometry [3]–[5], [8], [21]–[24] and ranging [11], [25]–[30], here, vibrometry is elaborated in the time domain of the intermediate frequency (IF) signal. This allows for fast-time[1] measurement of vibration displacements with a significantly higher measurement rate compared with the ramp-repetition rate. Instead of measuring only in the region of a few Hz, it allows us to measure at least the entire audio range of 16 kHz. The proposed measurement principle does not require super-fast frequency chirps. Usually, these chirps are noisy and nonlinear, e.g., due to the large loop bandwidth of the phase-locked loop (PLL) [31], which is commonly used for frequency synthesis. For a better understanding, Fig. 1 shows the difference between slow- and fast-time measurements.

Compared with unmodulated continuous-wave (CW) radar, which is widely used for radio wave vibrometry [16], [19], [32]–[38], fast-time vibrometry using FMCW radar generally enables simultaneous measurements of multiple vibrating radar targets by separating them within the range domain, which is the radial distance from the radar sensor to the

---

[1]Slow time: with chirp repetition rate $1/T$ and fast time: with analog-to-digital converter sampling rate f_s.

respective target. Generally, CW radar does not allow measuring distances unambiguously within the entire measurement range. Also, multiple reflecting radar targets cannot be separated. However, there are enhanced CW techniques that can partially overcome these restraints. For example, phase-comparison monopulse radar [15] or adaptive beam steering [37] could separate multiple targets based on their angular location, and multitone CW radar [38] could enhance the range unambiguity. FMCW radar does not have these restraints. Its measurement principle is unambiguous, and multiple targets can be separated according to the available bandwidth. Nevertheless, compared with CW radars, the hardware of FMCW radars is more complex and more expensive. However, as frequency increases up to mmWave and the lower THz range, these systems could be entirely on-chip, thus significantly reducing the price. Rodenbeck *et al.* [39] demonstrated a procedure for remote sensing of vibrating radar targets in motion using mmWave pulse-Doppler radar. Their approach also works in fast time, and they also use continuous motion compensation techniques. However, compared with pulse (Doppler) radar, an FMCW radar has a low peak power and can therefore be integrated into low-cost radar systems with ultrahigh bandwidth.

This article is an extension of [40], where we demonstrated a basic working principle of fast time, i.e., intrachirp vibrometry using the FMCW radar. This extended article consists of an in-depth investigation of the following features. We derived a sophisticated error model, which accurately describes the effects of the radar hardware on vibrometry and ranging accuracy. Furthermore, we present two signal processing chains for fast-time vibrometry and slow-time ranging, respectively. The slow-time measurement principle is based on a highly accurate phase evaluation [25]–[27], [41], [42], which we elaborated in [25]. Then, the methods of vibrometry and ranging are used together as a combined measuring procedure for measuring multiple vibrating radar targets in motion. As a consequence, a two-step technique for continuous self-calibration is necessary and will be introduced. After that, we propose an additional calibration technique, which is performed in the baseband and does not require any radio frequency (RF) metrology. Compared with conventional calibration methods, it provides the calibration of the radar, considering the propagation delay independent and dependent RF phase response, where the latter is primarily due to nonlinearities of the frequency ramp synthesizer. Fig. 2(a) and (b) shows a photograph of the experimental setup and the related results of our prior work, which is extended here. They clearly illustrate that we could measure the vibration frequencies of multiple nonmoving but simultaneously vibrating radar targets in fast time.

To demonstrate the proposed calibration and measurement methods, we utilized three ultrawideband FMCW radar systems, which cover the mmWave spectrum. The RF front ends [23], [43], [44] of these radar systems are still milestones regarding relative bandwidth and phase noise. Then, we utilized an experimental setup, where an adjustable vibrating radar target was moved along the 5-m linear rail.

Our article is a proof of concept for a new measurement technique, whose potential application is real-time and
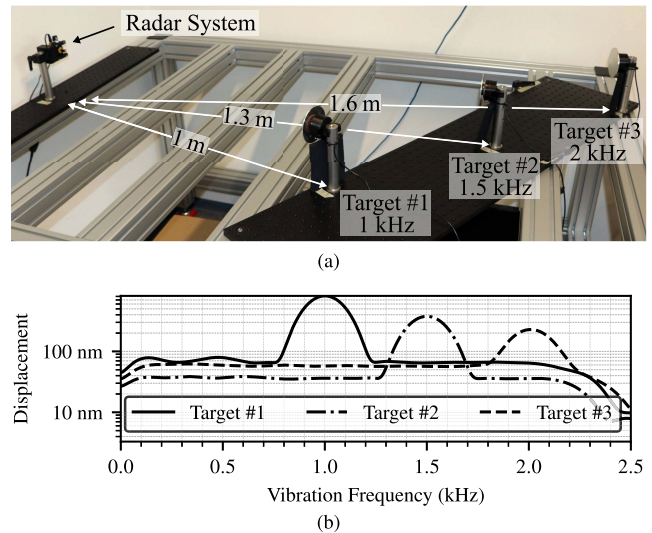

Fig. 2. Photograph and results of the experiments in our previous work [25]. It demonstrates the capability of measuring multiple simultaneously vibrating radar targets with fast-time vibrometry using the FMCW radar. We utilized an 80-GHz radar with 24-GHz bandwidth. (a) Experimental setup. (b) Experimental results.

in-process monitoring of industrial production processes, e.g., in machine tools. A fusion of micrometer accurate ranging and highly precise vibrometry is applicable for accurate adjustment of the machine parameters and condition monitoring for indicating wear. Machines produce transient and continuous acoustic emissions during operation, whose characteristic frequency signature can be identified using machine learning and pattern recognition to indicate the tool lifetime or the machine state. Due to an increasing lack of resources and growing environmental awareness, defective machines, or worn-out tools, which cause faulty workpieces, are of particular importance. In addition, machine downtimes can be reduced, thus increasing production efficiency.

The organization of this article is as follows Section II addresses the necessary fundamentals and introduces an error model for highly accurate ranging and vibrometry using the FMCW radar. Section III describes the proposed signal processing methods for slow-time ranging and fast-time vibrometry. Section IV demonstrates the experimental results using three radar systems covering the mmWave spectrum. Finally, Section V concludes this article.

The following notation is used for variables. Complex-valued variables, such as analytic signals, are written with an underscore (e.g., $\underline{s}_{\text{if}}(t)$). Matrices and column vectors are written as boldface upper (e.g., $\boldsymbol{E}$) and lower cases (e.g., $\boldsymbol{\epsilon_0}$), respectively.

II. DISTANCE ESTIMATION USING FMCW RADAR

A. FMCW Radar Fundamentals

FMCW radar systems use electromagnetic waves to determine the range, velocity, and angle of reflecting objects. Fig. 3 shows a generalized schematic of the monostatic[2] linear

---

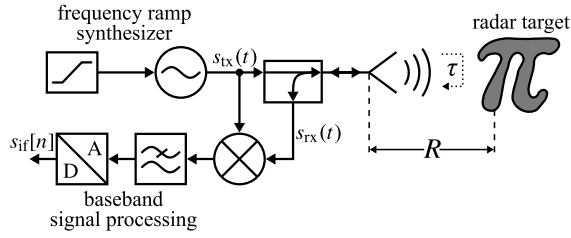[2]Transmitter and receiver are colocated (transceiver).

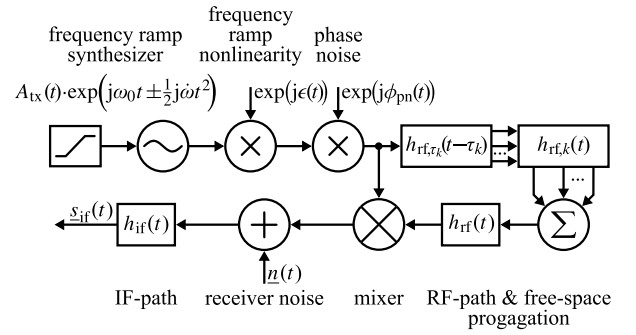Fig. 3.   Schematic of the monostatic FMCW radar principle.

Fig. 4.   Signal flow diagram of the generalized error model for highly accurate ranging and vibrometry with ultrawideband FMCW radar using complex-valued analytic signals.

FMCW (LFMCW) principle, as used here. A frequency ramp synthesizer generates a linear frequency-modulated signal, which is also called frequency ramp or frequency chirp

$$s_{\text{tx}}(t) = A_{\text{tx}} \cdot \cos\left(\omega_0 t + \int \pm \dot{\omega} t \, dt\right), \quad -\frac{T}{2} \le t \le \frac{T}{2}. \quad (1)$$

The center angular frequency is given by ω_0, and the ramp slope is given by $\dot{\omega} = B/T$, of which B is the ramp bandwidth in radians per second and T is the ramp sweep time. The parameter A_{tx} is the amplitude of the transmit signal. For the sake of convenience, "$\pm$" or "$\mp$" in all following equations applies to upchirp or downchirp, respectively. The signal in (1) is redefined as

$$s_{\text{tx}}(t) = A_{\text{tx}} \cdot \cos\left(\omega_0 t \pm \frac{1}{2}\dot{\omega} t^2\right) \quad (2)$$

and radiated via a coupler or circulator into free space using an antenna. Here, the electromagnetic wave impinges among reflecting objects, the so-called radar targets. The receive signal for a single idealized point scattering radar target is damped to A_{rx} and delayed by τ copy of the transmit signal $s_{\text{tx}}(t)$

$$s_{\text{rx}}(t) = A_{\text{rx}} \cdot \cos\left(\omega_0 \cdot (t - \tau) \pm \frac{1}{2}\dot{\omega} \cdot (t - \tau)^2\right). \quad (3)$$

After the reception, a homodyne receiver compares $s_{\text{tx}}(t)$ and $s_{\text{rx}}(t)$. Assuming that K radar targets result in a superposition of K quasi sinusoidal beat signals within the baseband

$$s_{\text{if}}(t) = \sum_{k=0}^{K-1} A_k \cdot \cos\left(\dot{\omega}\tau_k t \pm \omega_0 \tau_k - \frac{1}{2}\dot{\omega}\tau_k^2\right) \quad (4)$$

the so-called IF signal. The IF signal is characterized by the parameters amplitude A_k and propagation delay τ_k. Both frequency and phase of the particular signal component are proportional to the propagation delay τ. The distance from the radar to the respective target is indicated by $\tau c/2$, where c is the propagation speed of electromagnetic waves.

B. Proposed Error Model

However, each highly linear and low-noise radar system is impaired by perturbations of the hardware and dispersive free-space propagation. Consequently, this results in inaccurate and imprecise[3] range measurements as well as false detections due to indistinguishable ghost targets. To overcome this problem, we derive a sophisticated device error model, which is

then used for compensation to improve ranging in terms of measurement accuracy and precision. Especially with fast-time measurements as proposed here, compensation of RF phase perturbations is immanent. In contrast to (2), a more accurate model for the transmit signal is

$$s_{\text{tx}}(t) = A_{\text{tx}}(t) \cdot \cos\left(\omega_0 t \pm \frac{1}{2}\dot{\omega} t^2 + \epsilon(t) + \phi_{\text{pn}}(t)\right). \quad (5)$$

Due to the variation of the transmission power, the amplitude of the radiated wave $A_{\text{tx}}(t)$ cannot be assumed constant. It depends on the frequency in the RF path and, hence, on the sweep time t. The instantaneous phase is modulated by a perturbing component $\epsilon(t)$ due to nonlinearities of the frequency ramp, leading to systematic frequency deviations of the frequency chirp. In addition, the frequency ramp is affected by phase noise $\phi_{\text{pn}}(t)$ of the frequency synthesizer. The perturbed receive signal for K radar targets is

$$s_{\text{rx}}(t) = s_{\text{tx}}(t) * \left(\sum_{k=0}^{K-1} h_{\text{rf},\tau_k}(t - \tau_k) * h_{\text{rf},k}(t)\right) * h_{\text{rf}}(t) \quad (6)$$

as shown in Fig. 4. The receive signal is a convolution of the transmit signal $s_{\text{tx}}(t)$ with a propagation delay-dependent impulse response of the RF path $h_{\text{rf},\tau_k}(t)$, where τ_k is the propagation delay of the respective target. In particular, with ultrawideband radar systems in the presence of adjacent and sharp absorption lines of gas molecules, $h_{\text{rf},\tau_k}(t)$ represents these perturbing propagation effects. Oxygen and water vapor components in the atmosphere could affect radio waves when measuring within the mmWave region.[4] In addition, the signal is convolved with $h_{\text{rf},k}(t)$, which is the impulse response of the respective radar target. It expresses the near-field effects of nonpoint-shaped targets or radar targets with multiple inseparable scattering points due to insufficient radar bandwidth. As investigated in [25], $h_{\text{rf},k}(t)$ refers to the variation of the target phase center. Especially with highly accurate ranging over a broad range, variation of $h_{\text{rf},k}(t)$ becomes crucial. The last component within the RF path impulse response is $h_{\text{rf}}(t)$, which defines radar hardware-related perturbations between the mixer and the antenna. It represents antenna ringing, crosstalk within the radar hardware, and dispersion

---

[3]Precision: random errors and accuracy: systematic errors.

[4]Important molecular absorption lines in air within the mmWave spectrum: O_2: 60 and 119 GHz, and H_2O: 22, 183, and 325 GHz [45].

$A \cdot \exp\left(j\left(\dot{\omega}\tau t \pm \omega_0 \tau - \frac{1}{2}\dot{\omega}\tau^2\right)\right)$

$A_\epsilon(t) \cdot \exp\left(\mp j(\epsilon_0(t) + \epsilon_1(t)\tau)\right)$ $\exp(j\phi_{\mathrm{pn},\tau}(t))$ $\underline{n}(t)$

amplitude & phase modulation   phase noise   receiver noise   IF-path
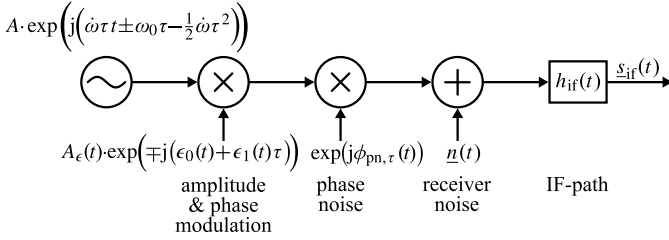
$\underline{s}_{\mathrm{if}}(t)$

Fig. 5. Equivalent error model for a single radar target in baseband representation.

in waveguides or striplines. The static nonlinear device error model for the IF signal is

$$s_{\mathrm{if}}(t) = \big(s_{\mathrm{tx}}(t) \cdot s_{\mathrm{rx}}(t) + n(t)\big) * h_{\mathrm{if}}(t) \qquad (7)$$

where the homodyne receiver generates the beat signal. In contrast to (4), the IF signal is perturbed by additive white Gaussian noise $n(t)$. It unifies the hardware immanent receiver noise of the RF components, such as the mixer, amplifier or coupler, thermal noise, and noise within the baseband signal processing like quantization noise of the analog-to-digital converter. The signal is convolved with the impulse response of the IF path $h_{\mathrm{if}}(t)$ due to the IF filter. Consequently, this leads to a frequency and, thus, range-dependent variation of the IF signal parameters amplitude and phase.

The representation of the device model in the RF domain is difficult to characterize. Therefore, we propose a generalized device model in baseband representation, which is equivalent to the model, as described before. This kind of representation is well suited for simulation of a discrete quantity of radar targets. Fig. 5 shows the error model using complex-valued analytic signals. We redefine (7) for K radar targets by

$$
\begin{aligned}
&s_{\mathrm{if}}(t) \\
&= \left(\sum_{k=0}^{K-1} A_k A_\epsilon(t) \cdot \cos\big(\phi_k(t) + \phi_{\mathrm{pn},\tau_k}(t)\big) + n(t)\right) * h_{\mathrm{if}}(t).
\end{aligned}
$$
$$(8)$$

The signal consists of a superposition of a sinusoid for each scatterer. Unchanged to (7), it is affected by additive white Gaussian noise and the IF path impulse response. The amplitude is composed of two components A_k and $A_\epsilon(t)$, where A_k represents the free-space path lost and the radar cross section (RCS). It is given by the radar range equation for far-field conditions, as considered in $h_{\mathrm{rf},\tau_k}(t)$ and $h_{\mathrm{rf},k}(t)$. The amplitude modulation component $A_\epsilon(t)$ covers $A_{\mathrm{tx}}(t)$ and the attenuation in $h_{\mathrm{rf}}(t)$, e.g., due to dispersive components or even amplitude modulation by dispersive wave propagation in free space. In addition, phase noise $\phi_{\mathrm{pn},\tau_k}(t)$ perturbs the instantaneous phase, which is $\phi_{\mathrm{pn}}(t) - \phi_{\mathrm{pn}}(t - \tau)$. Due to correlation effects in the homodyne transceiver, the phase noise of the phase noise source partially cancels out depending on the propagation delay of the radiated wave τ. According to [46], the single-sided phase noise spectrum in the IF signal is

$$\mathcal{L}_{\mathrm{if},\tau}(\omega) = \mathcal{L}(\omega) + 20\log_{10}\big(2\sin(\omega\tau)\big) \qquad (9)$$

where $\mathcal{L}(\omega)$ is the single-sided power spectral density (PSD) of the phase noise generated by the frequency ramp source.

The intermediate phase

$$\phi_k(t) = \dot{\omega}\tau_k t \pm \omega_0 \tau_k - \frac{1}{2}\dot{\omega}\tau_k^2 \mp \epsilon_0(t) \mp \epsilon_1(t)\tau_k \qquad (10)$$

which carries the frequency and zero-phase information, is disturbed by two parameters $\epsilon_0(t)$ and $\epsilon_1(t)$. The first parameter

$$\epsilon_0(t) = \arg\big\{\underline{H}_{\mathrm{rf}}(j\omega)\big\} + \arg\big\{\underline{H}_{\mathrm{rf},k}(j\omega)\big\}, \quad \text{with } \omega = \omega_0 \pm \dot{\omega}t \qquad (11)$$

defines the entire phase response of the RF path, which is independent of the propagation delay τ. Since

$$\lim_{\tau \to 0} \frac{\epsilon(t) - \epsilon(t - \tau)}{\tau} = \frac{\mathrm{d}}{\mathrm{d}t}\epsilon(t). \qquad (12)$$

is applicable, the second parameter $\epsilon_1(t)$ is

$$\epsilon_1(t) = \frac{\arg\big\{\underline{H}_{\mathrm{rf},\tau}(j\omega)\big\}}{\tau} - \frac{\mathrm{d}}{\mathrm{d}t}\epsilon(t), \quad \text{with } \omega = \omega_0 \pm \dot{\omega}t \qquad (13)$$

which summarizes nonlinearities of the frequency ramp and the distance-dependent RF path phase responses, due to molecular absorption lines. Hence, $\epsilon_1(t)\tau$ is the deviation of the instantaneous phase and $\epsilon_1(t)$ is the deviation of the instantaneous frequency in radians per second.

III. PROPOSED SIGNAL PROCESSING METHODS

A. Slow-Time Ranging

A basic method commonly used for slow-time range estimation using FMCW radar systems is calculating the discrete Fourier transform (DFT) of the IF signal $s_{\mathrm{if}}[n]$, followed by a maximum peak detection within the magnitude spectrum. Nevertheless, this approach is very inaccurate and imprecise. Zero padding or parabolic interpolation is commonly used to improve the spectral estimation. These simple treatments are just as imprecise and do not consider radar hardware impairments or effects through near-field wave propagation, as elaborated in Section II-B. In the following, we introduce an enhanced procedure for sinusoidal parameter and range estimation, which is then used together with the signal processing approach for fast-time vibrometry, as shown in Section III-B. The slow-time procedure is similar to the enhanced phase evaluation, which we have introduced in [25]. We implemented changes in the RF path compensation and absolute phase estimation, which reduces the computational load. The signal processing method combines a time-domain[5] impulse measurement principle (IF evaluation) with an interferometric measurement principle (IF signal zero-phase evaluation). It allows a very precise and unambiguous range estimation with the highest accuracy.

Fig. 6 roughly shows the algorithm for slow-time sinusoidal parameter and range estimation. First, the time-centered fast Fourier transform (FFT), a calculation-optimized version of the DFT, is

$$
\underline{S}_{\mathrm{if}}[n] = \begin{cases} \mathrm{FFT}\{s_{\mathrm{if}}[n + N/2] \cdot w[n]\}, & n = 0, 1, \ldots, N/2 - 1 \\ \mathrm{FFT}\{s_{\mathrm{if}}[n - N/2] \cdot w[n]\}, & n = N/2, \ldots, N - 1 \end{cases}
$$
$$(14)$$

[5]The magnitude spectrum of the FMCW IF signal is approximately the time-domain radar impulse response.
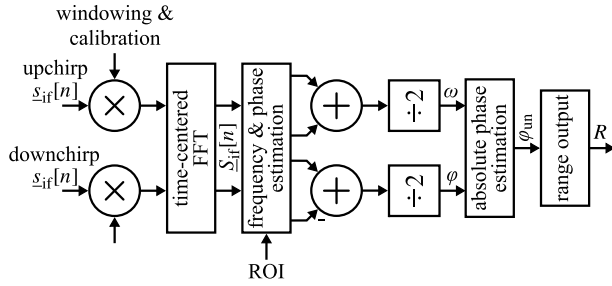
Fig. 6.   Flow diagram of the slow-time ranging approach. Adjacent IF signals of upchirp and downchirp are processed together for further accuracy improvements.

where N is the number of data samples and $w[n]$ is the window function, which is highly beneficial in spectral analysis. A Von-Hann[6] window is a good compromise between sidelobe suppression and unwanted main-lobe broadening. The time-centered FFT places the time origin ($t = 0$) to the centered FFT bin. A general nontime-centered FFT would cause a group delay of $T/2$. Within the predefined range of interest (ROI), a rough bin estimate, i.e., a frequency estimate, is

$$\hat{n} = \underset{n \in \text{ROI}}{\arg \max} \ |\underline{S}_{\text{if}}[n]|. \tag{15}$$

An interpolation function is used to improve the frequency resolution with the coarse grid of bins. The exponential parabolic interpolation

$$n = \hat{n} - \frac{|\underline{S}_{\text{if}}[\hat{n}]|^p - |\underline{S}_{\text{if}}[\hat{n}+1]|^p}{2|\underline{S}_{\text{if}}[\hat{n}]|^p - |\underline{S}_{\text{if}}[\hat{n}+1]|^p - |\underline{S}_{\text{if}}[\hat{n}-1]|^p} + \frac{1}{2} \tag{16}$$

as introduced in [47], perfectly increases the FFT resolution. The parameter p is chosen depending on the spectral pulse shape, i.e., according to the window function.[7] The interpolated bin is then used to calculate a frequency estimate ω within the magnitude spectrum $|\underline{S}_{\text{if}}[n]|$ and a phase estimate within the phase spectrum $\arg\{\underline{S}_{\text{if}}[n]\}$, which is ambiguous within $[-\pi, \pi]$. In the phase spectrum, local phase unwrapping[8] followed by linear interpolation is advantageous. The evaluation steps are repeated twice for each adjacent pair of upchirp and downchirp, assuming triangular frequency chirps. These frequency estimates are combined

$$\omega = \frac{\omega_{\text{up}} + \omega_{\text{down}}}{2} \tag{17}$$

which cancels out the Doppler effect for a uniformly moving radar target. The previously estimated phases for upchirp and downchirp are processed similarly

$$\varphi = \frac{\varphi_{\text{up}} - \varphi_{\text{down}}}{2}. \tag{18}$$

Since the particular zero phases are not affected by a Doppler shift, the reason for this operation is to cancel out phase shifts caused by the IF path pulse response $H_{\text{if}}(t)$ and the residual τ^2 zero-phase shift in (8) and (10). A combination of frequency and phase estimation is necessary, whereas φ is unambiguous

[6]A raised cosine function usually called Hanning window.
[7]Rectangular: $p = 0.78$ and Von-Hann: $p = 0.23$ [47].
[8]Phase unwrapping is the reconstruction of a sequence of phase values from their modulo 2π values.

within a range of π. Hence, the unambiguous phase within the entire measurement range is

$$\varphi_{\text{un}} = \varphi + \left\lfloor \frac{\omega \frac{\omega_0}{\dot{\omega}} - \varphi}{\pi} \right\rceil \cdot \pi \tag{19}$$

where $\lfloor \cdot \rceil$ denotes rounding to the nearest integer. Then, the slow-time range estimation becomes

$$R = \frac{\varphi_{\text{un}}}{\omega_0} \cdot \frac{c}{2}. \tag{20}$$

The Cramér–Rao bound (CRB) expresses a lower bound for the efficiency of unbiased estimators $\text{CRB}(\cdot) \leq \text{Var}(\cdot)$. Assuming that $s_{\text{if}}[n]$ is embedded in white Gaussian noise, then the CRB for phase evaluation is (see [25])

$$\text{CRB} \ R = \frac{c^2}{4\eta N \omega_0^2} \tag{21}$$

where η is the linear signal-to-noise ratio (SNR). Considering [25], the CRB is $12/B_{\text{rel}}^2$ times smaller than the generally used frequency evaluation with maximum peak detection in the spectrum. The parameter $B_{\text{rel}} = B/\omega_0$ is the relative bandwidth of the radar sensor.

B. Fast-Time Vibrometry

Vibrometry using FMCW radar with spectral methods in slow-time is fundamentally limited by the ramp-repetition rate $1/T$. This means that the maximum measurable frequency using slow-time measurement is $1/(2T)$ and thus very low. This article introduces a signal processing approach for fast-time vibrometry using the FMCW radar to overcome the paradigm of signal processing within the slow-time range profile. Assuming a radar target in the distance R_0, which is superimposed by an oscillation with a frequency ω_{vib} and an amplitude ΔR

$$R(t) = R_0 + \Delta R \sin(\omega_{\text{vib}} t). \tag{22}$$

The target vibration is assumed to be radially oriented toward the radar. According to (4), the simplified IF signal is

$$\underline{s}_{\text{if}}(t) = \underline{\bar{s}}_{\text{if}}(t) \cdot \exp\left(j h B_{\text{rel}} \sin(\omega_{\text{vib}} t) \frac{t}{T} \pm j h \sin(\omega_{\text{vib}} t) \right) \tag{23}$$

with

$$\underline{\bar{s}}_{\text{if}}(t) = \exp\left(j \frac{2\dot{\omega} R_0}{c} t \pm j \frac{2\omega_0 R_0}{c} \right) \tag{24}$$

and

$$h = \frac{2\omega_0 \Delta R}{c}. \tag{25}$$

The IF signal $\underline{s}_{\text{if}}(t)$ is frequency modulated, where $\underline{\bar{s}}_{\text{if}}(t)$ is the carrier signal and h is the modulation index known from the communication theory. The first term $\exp(j h B_{\text{rel}} \sin(\omega_{\text{vib}} t) t/T)$ in (23) is negligible. Hence, the equation is reduced to

$$\underline{s}_{\text{if}}(t) = \underline{\bar{s}}_{\text{if}}(t) \cdot \exp\left(\pm j h \sin(\omega_{\text{vib}} t) \right). \tag{26}$$

Fig. 7 shows the signal processing chain for fast-time vibrometry, which consists of a two-step self-calibration procedure, which significantly improves the quality of measurement.
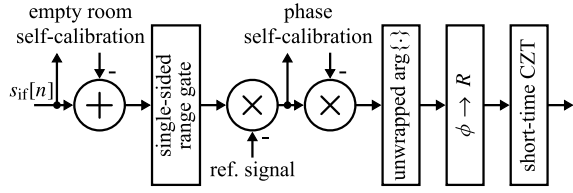
Fig. 7. Flow diagram of the signal processing chain for fast-time vibrometry. Empty-room self-calibration and phase self-calibration belong to Fig. 9.

Instead of evaluating the spectrum within the entire sweep time, each fast-time sampling point of the instantaneous phase

$$\phi[n] = \arg\left\{\frac{(s_{\text{if}}[n] - s_{\text{rcal}}[n]) * rg[n]}{\underline{s}_{\text{ref}}[n] \cdot \underline{s}_{\text{pcal}}[n]}\right\} \tag{27}$$

is processed individually. Equation (27) denotes the entire procedure for estimating the instantaneous phase $\phi[n]$, of which the details are as follows.

1) *Reference Signal and Frequency Conversion:* Fast-time measurement requires a reference signal

$$\underline{s}_{\text{ref}}[n] = A \cdot A_\epsilon[n] \cdot \exp\left(j(\omega t_n + \varphi \mp \epsilon_0[n] \mp \epsilon_1[n]\tau)\right) \tag{28}$$

used for frequency conversion similar to the carrier signal within frequency modulation in communication technology. The sinusoidal parameters A, ω, φ, and the propagation delay τ are estimated in a prior slow-time measurement, and $A_\epsilon[n]$, $\epsilon_0[n]$, and $\epsilon_1[n]$ are determined within a calibration process described later in Section III-C. The variable t_n subsumes

$$t_n = \frac{n}{f_s} - \frac{T}{2}, \quad n = 0, 1, \ldots, N - 1. \tag{29}$$

2) *Single-Sided Range Gate:* A range gate is applied to restrain unwanted interfering targets and to increase the SNR by suppressing unneeded frequency components in the signal. Range gating is realized by multiplying the signal with the single-sided range gate function

$$rg[n] \; \overset{\mathcal{F}}{\circ\!\!-\!\!\bullet} \; RG[n] = \begin{cases} 1, & \forall \; |\omega - 2\pi f_n| \le \dfrac{\omega_{\text{rg}}}{2} \\ 0, & \text{otherwise} \end{cases} \tag{30}$$

in the frequency domain, where the variable f_n is

$$f_n = f_s \cdot \frac{n}{N} \quad n = 0, 1, \ldots, N - 1. \tag{31}$$

The single-sided range gate is a rectangular function shifted to ω with an IF bandwidth of ω_{rg}, which only passes positive frequency components. According to the Euler identity, leaving out the negative frequencies results in a complex-valued analytic signal, which is necessary to derive the instantaneous phase of the time-domain signal by applying the argument function $\arg\{\cdot\}$. The IF signal is frequency modulated, resulting in sidebands. For sinusoidal modulating signals, the spectrum of these sidebands can be expressed as a Fourier series

$$\exp\left(jh\sin(\omega_{\text{vib}}t)\right) = \sum_{n=-\infty}^{\infty} J_n(h) \cdot \exp(jn\omega_{\text{vib}}t) \tag{32}$$
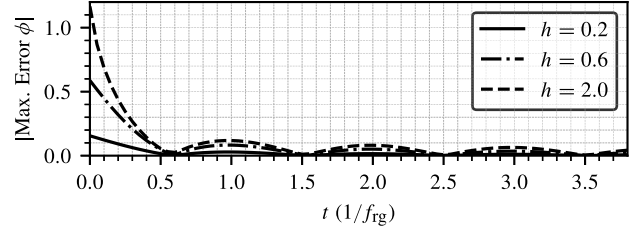

Fig. 8. Illustration of the maximum error on the left part of the instantaneous phase $\phi(t)$ due to range gating with a rectangular function. The parameter $h \propto \omega_0 \Delta R$ is the modulation index.
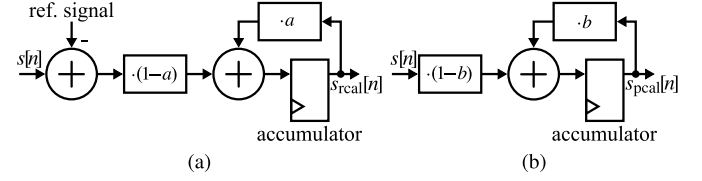

Fig. 9. Flow diagram of (a) continuous empty room and (b) continuous phase self-calibration methods.

where $J_n(\cdot)$ is the Bessel function first kind of order n. With Carson's bandwidth rule [48], a lower bound for the minimum required IF bandwidth of the range gate ω_{rg} to detect a certain vibration frequency ω_{vib}

$$\omega_{\text{rg}} \ge 2\omega_{\text{vib}} \cdot (h + 1) \tag{33}$$

is derived. The inequation is then reduced to

$$\omega_{\text{rg}} \ge 2\omega_{\text{vib}} \tag{34}$$

for a small modulation index h. Thus, the width of the range gate in meters is

$$R_{\text{rg}} \ge \omega_{\text{vib}} \cdot \frac{c}{\dot{\omega}} \tag{35}$$

which decreases by increasing the bandwidth B or reducing the sweeping time T of the frequency ramp. Range gating, i.e., limitation of the frequency components, leads to a significant error in the time domain. Edge effects or settling effects on the instantaneous phase are the consequence. Fig. 8 shows the maximum error of the instantaneous phase due to edge effects, considering the IF bandwidth of the range gate in Hz f_{rg} and the modulation index h. For each frequency ramp, at least the first and the last $0.5 \; f_s/f_{\text{rg}}$ samples of the instantaneous phase data should be discarded.

3) *Continuous Empty-Room Self-Calibration:* A continuous self-calibration method for the empty room is necessary to separate the wanted signal of the main target from surrounding interfering targets within the range gate. It must continuously adapt to the changing environment without suppressing the wanted signal. Fig. 9(a) shows the flow diagram for the continuous calculation of the empty-room calibration signal

$$\begin{aligned} s_{\text{rcal},m}[n] = \; & s_{\text{rcal},m-2}[n] \cdot a \\ & + (s_{m-1}[n] - s_{\text{ref},m-1}[n]) \cdot (1 - a) \end{aligned} \tag{36}$$

where m indicates the respective measurement cycle and a is a weighting coefficient for the accumulated calibration signal. A reference signal is deducted before accumulation to avoid the suppression of the wanted signal. With $a = 0.5$, we achieved excellent results in terms of a stable and fast calibration.

4) *Continuous Phase Self-Calibration:* An inadequate calibration of $\epsilon_0[n]$, $\epsilon_1[n]$, or a changing RF path pulse response, e.g., due to near-field effects or a hardware warmup, requires a continuous self-calibration of the intermediate phase. Fig. 9(b) shows the calculation procedure of the phase calibration signal

$$\underline{s}_{\mathrm{pcal},m}[n] = \underline{s}_{\mathrm{pcal},m-2}[n] \cdot b + \underline{s}_{m-1}[n] \cdot (1-b). \quad (37)$$

Again, with a weighting coefficient $b = 0.5$, we achieved good results for a stable and fast calibration.

Using the unwrapped intermediate phase, the estimate for the fast-time range variation is

$$R[n] = \frac{\phi[n]}{\dot{\omega}t_n \pm \omega_0} \cdot \frac{c}{2}. \quad (38)$$

The frequency components of $R[n]$ are now identified by Fourier analysis. Since the sampling rate $2\pi f_s$ is significantly higher than the IF bandwidth of the range gate ω_{rg}, which limits the upper detection bound, a chirp z-transform [49] is used to analyze a portion of the frequency components. To achieve a better sidelobe suppression, $R[n]$ needs to be windowed, e.g., with a Von-Hann window. In order to calculate the exact vibration amplitude, the processing gain as well as the coherent power gain of the window function [50] must be considered.

C. Estimation of the Calibration Parameters $\epsilon_0[n]$, $\epsilon_1[n]$, and $A_\epsilon[n]$

In this section, we demonstrate an approach to estimate the parameters $\epsilon_0[n]$, $\epsilon_1[n]$, and $A_\epsilon[n]$, as introduced in Section II-B. These variations from the ideal sinusoidal IF signal cause impairments of the peaks in the range profile. The parameters are crucial because they lead to inaccurate estimates in slow-time ranging or variations within the instantaneous phase in the fast-time vibrometry procedure. Since RF linearity measurements of ultrawideband radar systems are hard to carry out, our approach can also be used for estimating nonlinearities of the frequency ramp.

Fig. 10 shows the entire procedure for estimating the calibration parameters. A calibration parameter measurement series consists of M measurements that need to be executed consecutively with a single radar target at M arbitrary varying distances. The calibration signal is

$$\underline{s}[n] = \frac{s_{\mathrm{if}}[n] * rg[n]}{\exp\left(\mathrm{j}(\omega t_n + \varphi)\right)} \quad (39)$$

where the particular IF signals are range-gated and frequency-converted, as described in Section II-B. The system of linear equations is

$$\boldsymbol{\epsilon_0} + \boldsymbol{\epsilon_1} \cdot \boldsymbol{\tau}^{\mathrm{T}} = \boldsymbol{E} \quad (40)$$
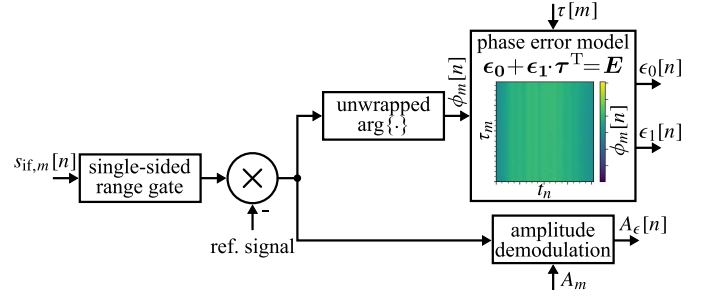

Fig. 10. Flow diagram for estimating the calibration parameters $\epsilon_0[n]$, $\epsilon_1[n]$, and $A_\epsilon[n]$.

where the regressand vectors $\boldsymbol{\epsilon_0}$ and $\boldsymbol{\epsilon_1}$ are

$$\boldsymbol{\epsilon_0} = [\epsilon_0[0], \dots, \epsilon_0[N-1]]^{\mathrm{T}} \quad (41)$$

and

$$\boldsymbol{\epsilon_1} = [\epsilon_1[0], \dots, \epsilon_1[N-1]]^{\mathrm{T}} \quad (42)$$

with the parameter vector

$$\boldsymbol{\tau} = [\tau_0, \dots, \tau_{M-1}]^{\mathrm{T}}. \quad (43)$$

The parameter τ_m is the propagation delay at the mth measurement point. The regressor matrix $\boldsymbol{E}$ containing the observations is

$$\boldsymbol{E} = \begin{bmatrix} \phi_0[0] & \cdots & \phi_{M-1}[0] \\ \vdots & \ddots & \vdots \\ \phi_0[N-1] & \cdots & \phi_{M-1}[N-1] \end{bmatrix} \quad (44)$$

where the input variables $\phi_m[n]$ denote the unwrapped instantaneous phase $\arg\{\underline{s}_m[n]\}$ of the mth measurement within the data set. To ensure the coherency of the unwrapping processes between the instantaneous phases over the entire data set, we recommend unwrapping by starting from the centered bin. This procedure ensures higher robustness against edge effects, as explained in Section III-B. The regressand variables $\epsilon_0[n]$ and $\epsilon_1[n]$ are then estimated, e.g., by linear regression.

Besides phase modulation, amplitude modulation is another primary source of radar imperfections. Especially for ultrawideband radar, this impairment becomes critical, e.g., due to a significant variation of the impedance by a mismatched antenna. The amplitude modulation is calculated as

$$A_\epsilon[n] = \frac{1}{M} \sum_{m=0}^{M-1} \frac{|\underline{s}_m[n]|}{A_m} \quad (45)$$

where the envelopes of the IF signals $|\underline{s}_m[n]|$ are divided by the respective amplitudes A_m, which are measured in slow-time before.

IV. EXPERIMENTAL RESULTS

A. Utilized Hardware and Calibration

As a test platform, we utilized three different radar systems, within a span from 68 to 250 GHz. These miniaturized ultrawideband FMCW radar systems are different in many ways. Thus, they have different impairments, which makes them
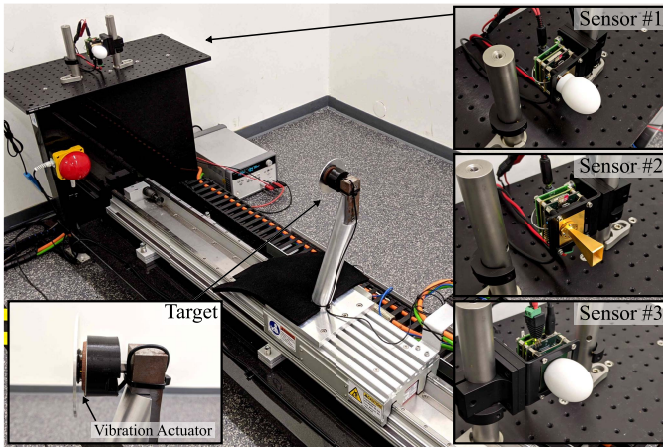
Fig. 11. Photograph of the experimental setup used to validate the proposed signal processing and calibration methods. We consecutively used three different mmWave radar sensors within the W-, D-, and Y-bands.

TABLE I
PARAMETERS OF THE RADAR SENSORS

Sensor	#1	#2	#3
Frequency range (GHz)	68...92	124...169	200...250
	(W-band)[a]	(D-band)	(Y-band)
Bandwidth (GHz)	24	45	50
Chirp rate (Hz)[b]		110	
Max. TX power (dBm)[c]	-4	-10	1.8
Phase noise (dBc/Hz)[d]	-85	-80	-75.6
Antenna	28 dBi lens	25 dBi	35 dBi lens
	WR-10 WG	rect. horn	bistatic
			on-chip patches
Operation mode		LFMCW	
Sampling rate[e]		1 MS/s	
Reference oscillator		OCXO (-105 dBc/Hz @10 Hz)	
Reference	[43], [51]	[23]	[44], [52]

[a] Sensor exceeds lower W-band specification by 7 GHz
[b] Measurement rate in slow-time
[c] Power at waveguide port / patch antenna EIRP
[d] @10 kHz offset to the center frequency
[e] Measurement rate in fast-time

perfectly suitable for demonstrating the calibration and measurement procedures. Table I shows the parameters of the radar sensors, whose RF hardware was developed by our group [23], [43], [44] using custom monolithic microwave integrated circuits (MMICs) in silicon–germanium (SiGe) technology. All sensors utilize an offset PLL technology for frequency synthesis. This technique provides the lowest phase noise and an excellent linearization of the PLL, resulting in especially linear frequency ramps. A low-noise oven-controlled crystal oscillator (OCXO) was used as a reference oscillator, which is highly frequency stable. Sensor #3 uses two bistatic on-chip antennas. Due to their close proximity and their shared lens, the system is considered as quasi-monostatic.

The chirp rate, which is the measurement rate in slow time, was 110 Hz, whereas the sampling rate was 1 MHz, which is the measurement rate in fast time. Considering the Nyquist–Shannon sampling theorem, the upper frequency limit for fast-time vibrometry is 0.5 MHz. However, it will be shown that the available SNR reduces this boundary. In contrast to fast-time vibrometry, the settling behavior of the PLLs limits the chirp rate and, hence, the frequency limit for slow-time vibrometry. An increase in the chirp rate would cause that the PLLs are no longer in lock.

Fig. 11 shows a photograph of the experimental setup. We used an aluminum disk with a diameter of 80 mm, attached to a vibration actuator, as a radar target. Moreover, the assembly is situated on a tilted bar, which is mounted onto a linear track. The linear track has a working range of at least 5 m. The vibration actuator is a 5-W voice coil, which can produce sounds at a moderate volume. The linear track has a positioning repeatability of about 10 μm. This setup is used for calibration with a step-by-step motion using the linear track. Alternatively, it provides an arbitrary large-scale motion, together with small-scale vibration, using the vibration actuators.

Fig. 12 shows the achieved calibrations for all sensors. The radar target was placed with an increment of 2.5 mm along the axis. We decided to limit the travel range from 1.5 to 5 m

in front of the sensors to ensure a point scatterer. At each calibration point, 50 upchirp and downchirp measurements were coherently averaged. The range gate was 10 kHz, which provides sufficient IF bandwidth to demonstrate the sensor impairments. This thorough procedure serves to illustrate the limits of the radar systems and can be significantly reduced in practical use by a factory preset. The figure is subdivided into calibration plots for each radar sensor, which shows $A_\epsilon[n]$, $\epsilon_0[n]$, and $\epsilon_1[n]$. The uncalibrated and calibrated echoes of the sensors are illustrated for demonstration. As shown in Fig. 12(n) and (o), the Y-band radar echo shows false pulses at half a distance due to parasitic radiation of the half transmit frequency [44].

The amplitude, hence the SNR of sensor #3, varies significantly with respect to the transmit frequency, as shown in Fig. 12(k). Fig. 12(b) shows the propagation delay-independent RF phase response $\epsilon_0[n]$ of the first sensor, which is mainly because of the highly dispersive waveguide used. In contrast to sensor #1, ringing due to internal reflections is the majority of $\epsilon_0[n]$ from sensor #2 and #3 [see Fig. 12(g), and (l)]. According to [45], the worst case variation of the dispersive delay due to absorption lines by gas molecules for the frequency range of the third sensor is less than 10 ps/km. This would cause a worst case error $\epsilon_1[n]$ not more than 0.75 MHz, fewer than shown in Fig. 12(m). The variation of the dispersive delay in the frequency range of sensor #1 and #2 is negligible. Therefore, we suppose that $\epsilon_1[n]$ [see Fig. 12(c), (h), and (m)] is an estimation for the nonlinearities of the frequency synthesizer.

Fig. 13 shows the measured noise floor in the vibration spectrum without any averaging to demonstrate the lower detection limit of each radar system at the given configuration. As known from the communication technology, there is a threshold effect for frequency modulation, which describes a significantly decreasing SNR if the carrier-to-noise ratio falls
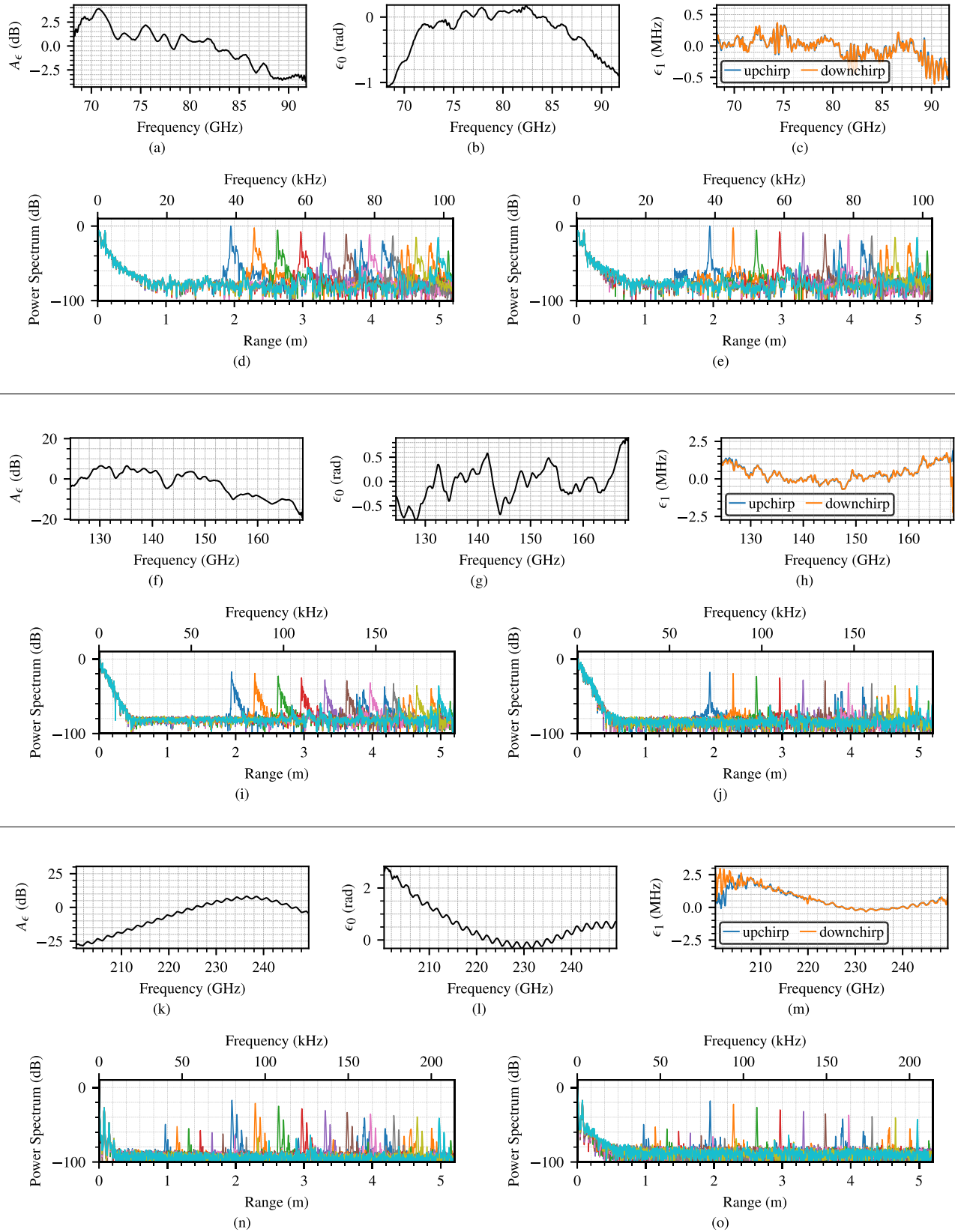
Fig. 12. Identified calibrations of the three radar sensors. The respective upper illustrations show A_ϵ, ϵ_0, and ϵ_1, whereas the lower illustrations show the normalized IF power spectrum before and after applying the calibration data. (a) Measured A_ϵ calibration of sensor #1. (b) Measured ϵ_0 calibration of sensor #1. (c) Measured ϵ_1 calibration of sensor #1. (d) Uncalibrated IF spectrum of sensor #1. (e) Calibrated IF spectrum of sensor #1. (f) Measured A_ϵ calibration of sensor #2. (g) Measured ϵ_0 calibration of sensor #2. (h) Measured ϵ_1 calibration of sensor #2. (i) Uncalibrated IF spectrum of sensor #2. (j) Calibrated IF spectrum of sensor #2. (k) Measured A_ϵ calibration of sensor #3. (l) Measured ϵ_0 calibration of sensor #3. (m) Measured ϵ_1 calibration of sensor #3. (n) Uncalibrated IF spectrum of sensor #3. (o) Calibrated IF spectrum of sensor #3.
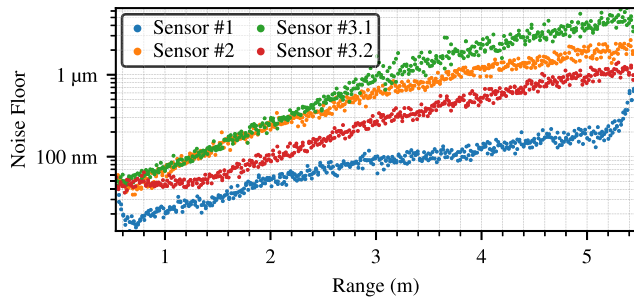
Fig. 13. Measured noise floor within the vibrometry spectrum of the three radar sensors. Sensor #3.1 and #3.2 belong to sensor #3 with a full or reduced number of sampling points to overcome the threshold effect for frequency modulation.

below a certain point. Due to the very low SNR, i.e., carrier-to-noise ratio, of the third radar sensor for the lower frequency range [see Fig. 12(k)], the respective noise floor is poor (see Sensor #3.1 in Fig. 13). Therefore, in the following, we reduced the sampling points of $R[n]$ to fit the RF range from 215 to 250 GHz. As a consequence, the noise floor could be improved significantly (see sensor #3.2 in Fig. 13). Since the shape of the radar target changes the RCS and, hence, the SNR, similar to a change in distance, it is unnecessary to investigate differently shaped radar targets in the subsequent experiments.

B. Vibrometry of a Fixed Radar Target

We did three vibrometry measurements without underlying large-scale motion. The radar targets were positioned at 1.3 m for sensor #1 and 0.5 m for sensor #2 and #3, thus providing sufficient SNR, according to Fig. 13. Reducing the range from the radar to the target would further limit the maximum IF bandwidth of the range gate and, hence, the upper limit of the detectable vibration frequency. A sequence of sinusoidal chirped vibrations was executed. The sequence took about 12 s and was within a frequency range of 300 Hz–16 kHz, covering the entire audio signal range. Sweeping through a single tone is sufficient to validate the proposed methods since a Fourier decomposition can represent complex vibrations as a sum of multitones.

Fig. 14 shows the experimental results. The entire frequency sweep is clearly visible. The noise floor is at 30 nm for the first and 50 nm for the second and third sensors. The figure shows the doubled-frequency components due to the harmonics of the audio power amplifier, which was used as a signal source. Smearing along the time axis, which appears with broadband events, e.g., the sudden shutdown of the vibration actuator, is due to the phase self-calibration. The mirrored ghost vibrations within Fig. 14(b) and (c) occurred because of multiple reflections, which are caused by ringing of the electromagnetic wave between the antenna and the target. Due to the short distance, the range gate cannot suppress these multiple reflections. These reflections are interfering targets, which are vibrating just as the main target. Consequently, they do not cancel out with the empty-room self-calibration.
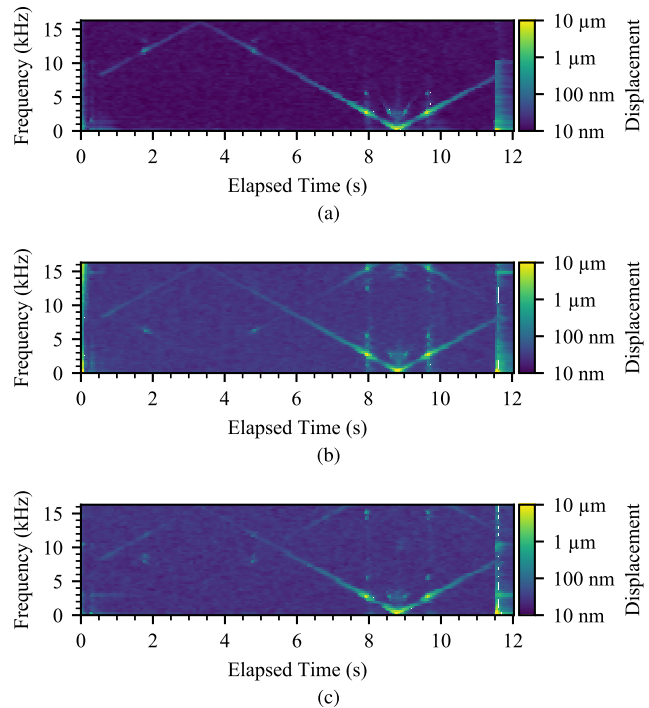

Fig. 14. Experimental results of the vibrometry measurements of a stationary radar target. The range of the vibration frequency is 300 Hz–16 kHz. (a) Fast-time vibrometry using sensor #1 with a radar target in $r = 1.3$ m. (b) Fast-time vibrometry using sensor #2 with a radar target in $r = 0.5$ m. (c) Fast-time vibrometry using sensor #3 with a radar target in $r = 0.5$ m.
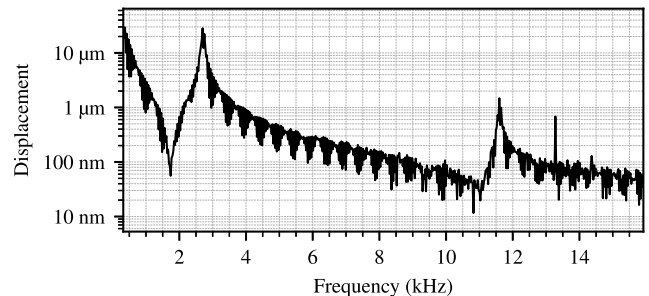

Fig. 15. Frequency response of the vibration actuator, which is obtained from the experimental result in Fig. 14. The resonance frequencies of the vibration actuator are evident.

Fig. 15 shows the frequency response of the vibration actuator. The frequency response was extracted from the linear chirp as shown in Fig. 14(a), where sensor #1 was used, which has the highest SNR. A highly nonlinear curve with resonance frequencies at 2.7 and 11.6 kHz is evident.

C. Vibrometry of a Radar Target in Motion

This section demonstrates the ability of the measurement approach to simultaneously detect vibrations in fast time together with an underlying large-scale motion. The vibration sequence was a triangular, followed by sinusoidal chirp, which took about 26 s in total. Compared with the previous experimental series, the upper limit of the frequency range
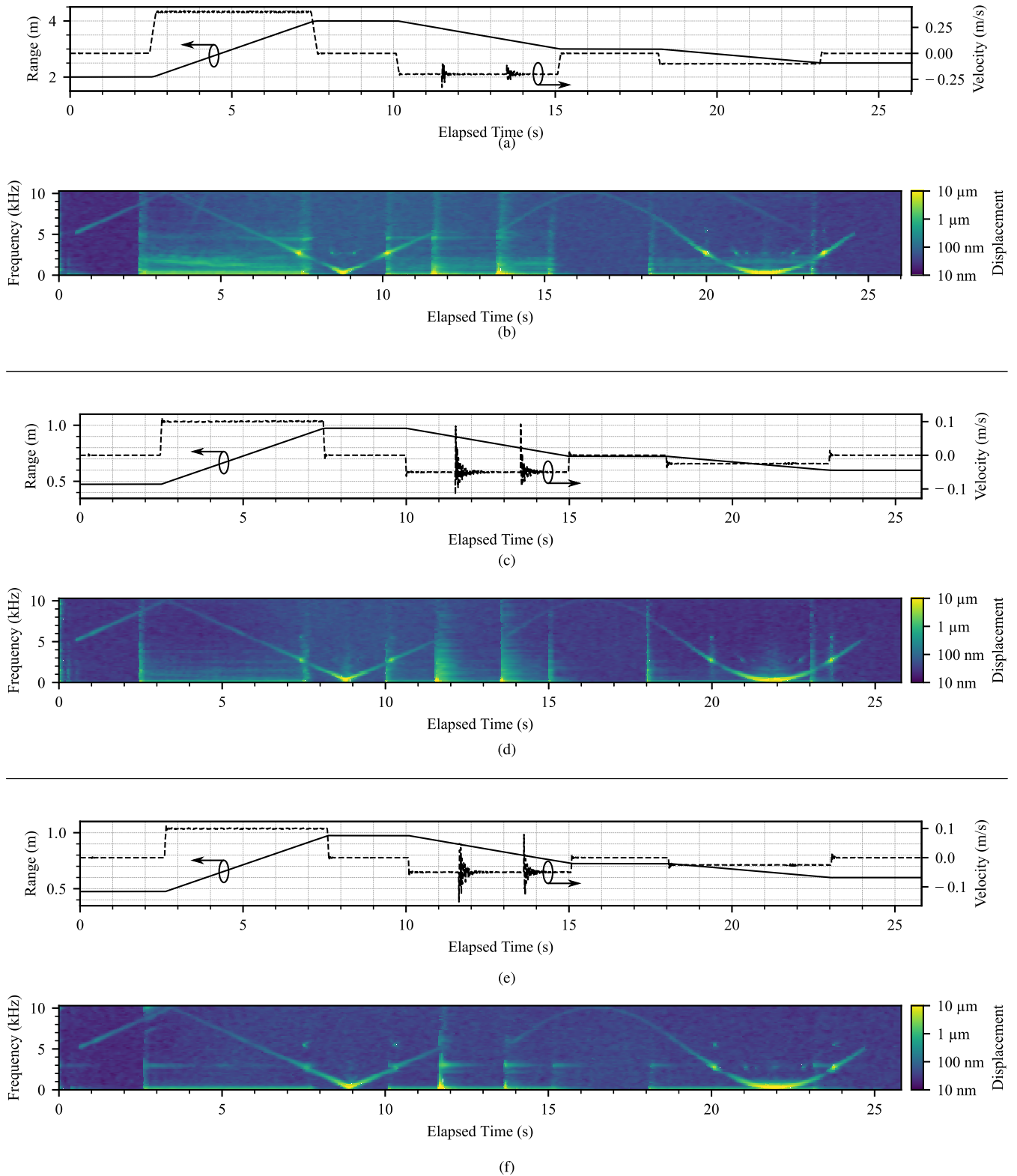
Fig. 16.   Experimental results for the vibrating radar target with an underlying large-scale motion. The upper plots show the slow time, whereas the lower plots show the fast-time measurement results. For slow-time ranging, the proposed phase evaluation approach was used. For velocity estimation, we used the Doppler frequency, which leads to a significant error for accelerated movements. (a) Slow-time ranging with sensor #1. (b) Fast-time vibrometry with sensor #1. (c) Slow-time ranging with sensor #2. (d) Fast-time vibrometry with sensor #2. (e) Slow-time ranging with sensor #3. (f) Fast-time vibrometry with sensor #3.
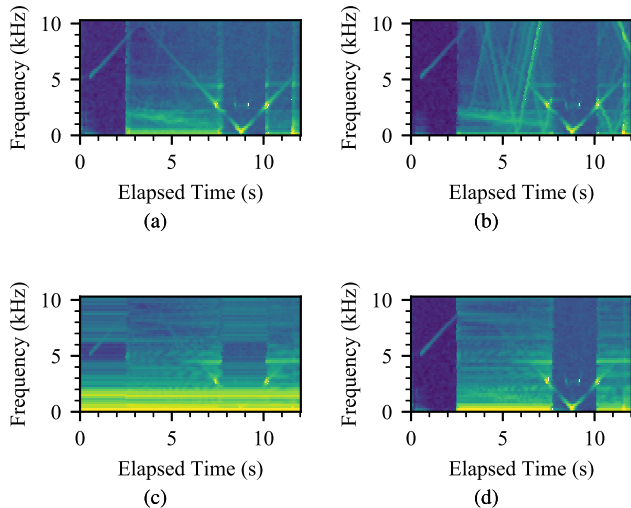
Fig. 17. Illustrations of the effectiveness of the calibration mechanisms using the experimental results from sensor #1 as shown in Fig. 16(b). The units are the same as in Fig. 16(b). (a) All calibration mechanisms are activated. (b) Without continuous empty-room self-calibration. (c) Without any phase calibration. (d) Without continuous phase self-calibration.

TABLE II
SUMMARY OF THE EXPERIMENTAL RESULTS

Sensor	#1	#2	#3
Common Slow-Time Vibrometry			
Max. detectable vibration frequency		55 Hz	
Proposed Fast-Time Vibrometry[a]			
Distance (m)	1.3	0.5	0.5
Min. detectable vibration displacement (nm)	30	50	50
Measured vibration frequency		16 kHz	
Proposed Fast-Time Vibrometry[b]			
Distance (m)	2...4	0.5...1	0.5...1
Large-scale motion (m/s)	0.4	0.1	0.1
Measured vibration frequency		10 kHz	

[a] Fixed radar target
[b] Radar target in motion

was reduced to 10 kHz. For sensor #1, the range of motion was within 4 m, whereas the velocity was up to 0.4 m/s. Again, to meet the SNR requirements, the range of motion for the second and third sensors was reduced to 1 m. Fig. 16 shows the measurement results. Fig. 16(a), (c), and (e) shows the results of slow-time ranging and velocity estimation, whereas Fig. 16(b), (d), and (f) shows the results of fast-time vibrometry. For slow-time ranging, phase evaluation was used, whereas the velocity was estimated using the Doppler estimation.

Accelerated movements highly disturb the Doppler estimation. However, using the proposed slow-time phase evaluation, the range measurements are not affected by this. Regarding vibrometry, the sequence of vibrations is clearly visible even if the radar target is within a fast movement. During motion, blurring is due to an insufficient continuous phase self-calibration and underlying vibrations by the moving linear actor. Fig. 16(b) shows a disturbing target within 20–25 s. This artifact is due to an imperfect empty-room self-calibration. Interfering targets occur as lines at frequencies, matching the IF signal frequency deviation between the main and the interfering target. Fig. 17 further shows the effect of the individual calibration mechanism. It shows a detailed view of the vibrometry plot of the first sensor with a moving radar target. The figure is divided into four subfigures, where specific calibration mechanisms are inactivated.

V. CONCLUSION

In this article, we proposed a sophisticated error model for highly accurate sensing using FMCW radar systems. We introduced a combined measurement approach for spatially resolved vibrometry and ranging of vibrating radar targets with underlying large-scale motions. Our novel signal processing chain in fast time allows sensing of significantly higher vibration frequencies than the chirp rate. Several simultaneously

vibrating targets or interfering targets could be unambiguously separated in the range domain in contrast to traditional CW radar sensors. Multiple calibration techniques were introduced to overcome the modeled imperfections in order to achieve these features.

We demonstrated the proposed techniques using three ultrawideband mmWave FMCW radar systems in the W-, D-, and Y-bands. The experimental results are shown in Table II. Vibrations up to 16 kHz with a displacement of a minimum of 30 nm could be measured, with a fixed radar target. Frequencies of at least 10 kHz were measured with a moving radar target of up to 0.4 m/s using the W-band sensor. We want to emphasize that with the commonly used slow-time measurements, only vibrations with frequencies up to 55 Hz could have been detected with the radar systems used. Consequently, we improved the upper detection limit for the vibration frequency by several orders of magnitude, which is outstanding in terms of spatially resolved vibrometry using FMCW radar systems.

REFERENCES

[1] J. G. Mueller and T. G. Pratt, "A radio frequency polarimetric sensor for rotating machine analysis," *IEEE Sensors J.*, vol. 13, no. 12, pp. 4866–4873, Dec. 2013.

[2] J. Hershberger, T. Pratt, and R. Kossler, "Non-contact rotating machine health status via dual-polarized radar," in *Proc. Texas Symp. Wireless Microw. Circuits Syst. (WMCS)*, Apr. 2018, pp. 1–6.

[3] J. Moll *et al.*, "Motion sensing of a wind turbine prototype using a bistatic FMCW Doppler radar sensor," in *Proc. 11th German Microw. Conf. (GeMiC)*, Mar. 2018, pp. 99–102.

[4] C. Zeintl, F. Eibensteiner, and J. Langer, "Evaluation of FMCW radar for vibration sensing in industrial environments," in *Proc. 29th Int. Conf. Radioelektronika (RADIOELEKTRONIKA)*, Apr. 2019, pp. 1–5.

[5] Z. Shao, X. Zhang, Y. Li, and J. Jiang, "A comparative study on radar interferometry for vibrations monitoring on different types of bridges," *IEEE Access*, vol. 6, pp. 29677–29684, 2018.

[6] J. Hu, J. Guo, L. Zhou, S. Zhang, M. Chen, and C. Hang, "Dynamic vibration characteristics monitoring of high-rise buildings by interferometric real-aperture radar technique: Laboratory and full-scale tests," *IEEE Sensors J.*, vol. 18, no. 15, pp. 6423–6431, Aug. 2018.

[7] M. Pieraccini, M. Fratini, F. Parrini, G. Macaluso, and C. Atzeni, "High-speed CW step-frequency coherent radar for dynamic monitoring of civil engineering structures," *Electron. Lett.*, vol. 40, no. 14, p. 907, 2004.

[8] G. Giunta *et al.*, "A novel technique for very accurate three-dimensional monitoring of structural vibrations and displacement by remote radar sensors," in *Proc. IET Int. Radar Conf.*, 2015, pp. 1–6.

[9] G. Luzi, M. Crosetto, and E. Fernández, "Radar interferometry for monitoring the vibration characteristics of buildings and civil structures: Recent case studies in spain," *Sensors*, vol. 17, no. 4, p. 669, Mar. 2017.

[10] C. Atzeni, A. Bicci, D. Dei, M. Fratini, and M. Pieraccini, "Remote survey of the leaning tower of pisa by interferometric sensing," *IEEE Geosci. Remote Sens. Lett.*, vol. 7, no. 1, pp. 185–189, Jan. 2010.

[11] M. Arsalan, A. Santra, and C. Will, "Improved contactless heartbeat estimation in FMCW radar via Kalman filter tracking," *IEEE Sensors Lett.*, vol. 4, no. 5, pp. 1–4, May 2020.

[12] C. Li, V. M. Lubecke, O. Boric-Lubecke, and J. Lin, "A review on recent advances in Doppler radar sensors for noncontact healthcare monitoring," *IEEE Trans. Microw. Theory Techn.*, vol. 61, no. 5, pp. 2046–2060, May 2013.

[13] H. Lee, B.-H. Kim, J.-K. Park, and J.-G. Yook, "A novel vital-sign sensing algorithm for multiple subjects based on 24-GHz FMCW Doppler radar," *Remote Sens.*, vol. 11, no. 10, p. 1237, May 2019.

[14] S. Kim and K.-K. Lee, "Low-complexity joint extrapolation-MUSIC-based 2-D parameter estimator for vital FMCW radar," *IEEE Sensors J.*, vol. 19, no. 6, pp. 2205–2216, Mar. 2019.

[15] S. M. M. Islam, O. Boric-Lubecke, and V. M. Lubecke, "Concurrent respiration monitoring of multiple subjects by phase-comparison monopulse radar using independent component analysis (ICA) with JADE algorithm and direction of arrival (DOA)," *IEEE Access*, vol. 8, pp. 73558–73569, 2020.

[16] D. Rodriguez and C. Li, "Sensitivity and distortion analysis of a 125-GHz interferometry radar for submicrometer motion sensing applications," *IEEE Trans. Microw. Theory Techn.*, vol. 67, no. 12, pp. 5384–5395, Dec. 2019.

[17] C.-S. Lin, S.-F. Chang, C.-C. Chang, and C.-C. Lin, "Microwave human vocal vibration signal detection based on Doppler radar technology," *IEEE Trans. Microw. Theory Techn.*, vol. 58, no. 8, pp. 2299–2306, Aug. 2010.

[18] M. Geiger, D. Schlotthauer, and C. Waldschmidt, "Improved throat vibration sensing with a flexible 160-GHz radar through harmonic generation," in *IEEE MTT-S Int. Microw. Symp. Dig.*, Jun. 2018, pp. 123–126.

[19] T.-Y.-J. Kao, A. Y.-K. Chen, Y. Yan, T.-M. Shen, and J. Lin, "A flip-chip-packaged and fully integrated 60 GHz CMOS micro-radar sensor for heartbeat and mechanical vibration detections," in *Proc. IEEE Radio Freq. Integr. Circuits Symp.*, Jun. 2012, pp. 443–446.

[20] E. Sazonov, H. Li, D. Curry, and P. Pillay, "Self-powered sensors for monitoring of highway bridges," *IEEE Sensors J.*, vol. 9, no. 11, pp. 1422–1429, Nov. 2009.

[21] L. Ding, M. Ali, S. Patole, and A. Dabak, "Vibration parameter estimation using FMCW radar," in *Proc. IEEE Int. Conf. Acoust., Speech Signal Process. (ICASSP)*, Mar. 2016, pp. 2224–2228.

[22] F. Hau, F. Baumgartner, and M. Vossiek, "Influence of vibrations on the signals of automotive integrated radar sensors," in *IEEE MTT-S Int. Microw. Symp. Dig.*, Mar. 2017, pp. 159–162.

[23] T. Jaeschke, C. Bredendiek, S. Kuppers, and N. Pohl, "High-precision D-band FMCW-radar sensor based on a wideband SiGe-transceiver MMIC," *IEEE Trans. Microw. Theory Techn.*, vol. 62, no. 12, pp. 3582–3597, Dec. 2014.

[24] Y. Xiong, Z. Peng, G. Xing, W. Zhang, and G. Meng, "Accurate and robust displacement measurement for FMCW radar vibration monitoring," *IEEE Sensors J.*, vol. 18, no. 3, pp. 1131–1139, Feb. 2018.

[25] L. Piotrowsky, T. Jaeschke, S. Kueppers, J. Siska, and N. Pohl, "Enabling high accuracy distance measurements with FMCW radar sensors," *IEEE Trans. Microw. Theory Techn.*, vol. 67, no. 12, pp. 5360–5371, Dec. 2019.

[26] S. Ayhan, S. Scherr, P. Pahl, T. Kayser, M. Pauli, and T. Zwick, "High-accuracy range detection radar sensor for hydraulic cylinders," *IEEE Sensors J.*, vol. 14, no. 3, pp. 734–746, Mar. 2014.

[27] S. Scherr, S. Ayhan, B. Fischbach, A. Bhutani, M. Pauli, and T. Zwick, "An efficient frequency and phase estimation algorithm with CRB performance for FMCW radar applications," *IEEE Trans. Instrum. Meas.*, vol. 64, no. 7, pp. 1868–1875, Jul. 2015.

[28] N. Pohl, M. Gerding, B. Will, T. Musch, J. Hausner, and B. Schiek, "High precision radar distance measurements in overmoded circular waveguides," *IEEE Trans. Microw. Theory Techn.*, vol. 55, no. 6, pp. 1374–1381, Jun. 2007.

[29] P. V. Brennan, K. Nicholls, L. B. Lok, and H. Corr, "Phase-sensitive FMCW radar system for high-precision antarctic ice shelf profile monitoring," *IET Radar, Sonar Navigat.*, vol. 8, no. 7, pp. 776–786, Aug. 2014.

[30] A. Anghel, G. Vasile, R. Cacoveanu, C. Ioana, and S. Ciochina, "Short-range wideband FMCW radar for millimetric displacement measurements," *IEEE Trans. Geosci. Remote Sens.*, vol. 52, no. 9, pp. 5633–5642, Sep. 2014.

[31] D. Weyer *et al.*, "Design considerations for integrated radar chirp synthesizers," *IEEE Access*, vol. 7, pp. 13723–13736, 2019.

[32] X. Ma *et al.*, "Design of a 100-GHz double-sideband low-IF CW Doppler radar transceiver for micrometer mechanical vibration and vital sign detection," *IEEE Trans. Microw. Theory Techn.*, vol. 68, no. 7, pp. 2876–2890, Jul. 2020.

[33] C. Gu, T. Inoue, and C. Li, "Analysis and experiment on the modulation sensitivity of Doppler radar vibration measurement," *IEEE Microw. Wireless Compon. Lett.*, vol. 23, no. 10, pp. 566–568, Oct. 2013.

[34] R. Rakshit, D. Roy, and T. Chakravarty, "On characterization of vibration measurement using microwave Doppler radar," in *Proc. IEEE Sensors*, Oct. 2018, pp. 1–4.

[35] F. Barbon, G. Vinci, S. Lindner, R. Weigel, and A. Koelpin, "A six-port interferometer based micrometer-accuracy displacement and vibration measurement radar," in *IEEE MTT-S Int. Microw. Symp. Dig.*, Jun. 2012, pp. 1–3.

[36] G. Vinci *et al.*, "Six-port microwave interferometer radar for mechanical vibration analysis," in *Proc. Eur. Radar Conf. (EuRAD)*, Nuremberg, Germany, Oct. 2013, pp. 287–290.

[37] C.-M. Nieh, C. Wei, and J. Lin, "Concurrent detection of vibration and distance using unmodulated CW Doppler vibration radar with an adaptive beam-steering antenna," *IEEE Trans. Microw. Theory Techn.*, vol. 63, no. 6, pp. 2069–2078, Jun. 2015.

[38] C. Gu and J. Lien, "A two-tone radar sensor for concurrent detection of absolute distance and relative movement for gesture sensing," *IEEE Sensors Lett.*, vol. 1, no. 3, pp. 1–4, Jun. 2017.

[39] C. T. Rodenbeck, J. B. Beun, R. G. Raj, and R. D. Lipps, "Vibrometry and sound reproduction of acoustic sources on moving platforms using millimeter wave pulse-Doppler radar," *IEEE Access*, vol. 8, pp. 27676–27686, 2020.

[40] L. Piotrowsky, J. Siska, C. Schweer, and N. Pohl, "Using FMCW radar for spatially resolved intra-chirp vibrometry in the audio range," in *IEEE MTT-S Int. Microw. Symp. Dig.*, Aug. 2020, pp. 791–794.

[41] M. Scherhaufl, F. Hammer, M. Pichler-Scheder, C. Kastl, and A. Stelzer, "Radar distance measurement with viterbi algorithm to resolve phase ambiguity," *IEEE Trans. Microw. Theory Techn.*, vol. 68, no. 9, pp. 3784–3793, Sep. 2020.

[42] M. Z. Ikram, A. Ahmad, and D. Wang, "High-accuracy distance measurement using millimeter-wave radar," in *Proc. IEEE Radar Conf. (RadarConf)*, Apr. 2018, pp. 1296–1300.

[43] N. Pohl, T. Jaeschke, and K. Aufinger, "An ultra-wideband 80 GHz FMCW radar system using a SiGe bipolar transceiver chip stabilized by a fractional-N PLL synthesizer," *IEEE Trans. Microw. Theory Techn.*, vol. 60, no. 3, pp. 757–765, Mar. 2012.

[44] S. Thomas, C. Bredendiek, and N. Pohl, "A SiGe-based 240-GHz FMCW radar system for high-resolution measurements," *IEEE Trans. Microw. Theory Techn.*, vol. 67, no. 11, pp. 4599–4609, Nov. 2019.

[45] H. J. Liebe, "An updated model for millimeter wave propagation in moist air," *Radio Sci.*, vol. 20, no. 5, pp. 1069–1089, Sep. 1985.

[46] K. Thurn, R. Ebelt, and M. Vossiek, "Noise in homodyne FMCW radar systems and its effects on ranging precision," in *IEEE MTT-S Int. Microw. Symp. Dig.*, Jun. 2013, pp. 1–3.

[47] M. Gasior, "Improving frequency resolution of discrete spectra," Ph.D. dissertation, Dept. Elect. Eng., Automatics, Comput. Sci. Electron., AGH Univ. Sci. Technol., Kraków, Poland, 2006.

[48] J. R. Carson, "Notes on the theory of modulation," *Proc. IRE*, vol. 10, no. 1, pp. 57–64, Feb. 1922.

[49] L. Rabiner, R. Schafer, and C. Rader, "The chirp z-transform algorithm," *IEEE Trans. Audio Electroacoust.*, vol. 17, no. 2, pp. 86–92, Jun. 1969.

[50] F. J. Harris, "On the use of windows for harmonic analysis with the discrete Fourier transform," *Proc. IEEE*, vol. 66, no. 1, pp. 51–83, Jan. 1978.

[51] N. Pohl, T. Jaeschke, S. Kuppers, C. Bredendiek, and D. Nusler, "A compact ultra-wideband mmWave radar sensor at 80 GHz based on a SiGe transceiver chip (Focused session on highly-integrated millimeter-wave radar sensors in SiGe BiCMOS technologies)," in *Proc. 22nd Int. Microw. Radar Conf. (MIKON)*, May 2018, pp. 345–347.

[52] S. Thomas, C. Bredendiek, T. Jaeschke, F. Vogelsang, and N. Pohl, "A compact, energy-efficient 240 GHz FMCW radar sensor with high modulation bandwidth," in *Proc. German Microw. Conf. (GeMiC)*, Mar. 2016, pp. 397–400.

Nils Pohl (Senior Member, IEEE) received the Dipl.Ing. and Dr.Ing. degrees in electrical engineering from Ruhr University Bochum, Bochum, Germany, in 2005 and 2010, respectively.

From 2006 to 2011, he was a Research Assistant with Ruhr University Bochum, where he was involved in integrated circuits for millimeter-wave (mmWave) radar applications. In 2011, he became an Assistant Professor at Ruhr University Bochum. In 2013, he became the Head of the Department of mm-Wave Radar and High Frequency Sensors, Fraunhofer Institute for High Frequency Physics and Radar Techniques, Wachtberg, Germany. In 2016, he became a Full Professor of integrated systems with Ruhr University Bochum. He has authored or coauthored more than 100 scientific articles and has issued several patents. His current research interests include ultrawideband mmWave radar, design, and optimization of mmWave integrated SiGe circuits and system concepts with frequencies up to 300 GHz and above, as well as frequency synthesis and antennas.

Dr. Pohl is a member of Verband der Elektrotechnik Elektronik Informationstechnik (VDE), Informationstechnische Gesellschaft (ITG), European Microwave Association (EUMA), and Union Radio-Scientifique Internationale (URSI). He was a co-recipient of the 2009 EEEfCom Innovation Award, the 2012 EuMIC Prize, and the 2015 Best Demo Award of the IEEE Radio Wireless Week. He was a recipient of the Karl-Arnold Award of the North Rhine-Westphalian Academy of Sciences, Humanities and the Arts in 2013 and the IEEE MTT Outstanding Young Engineer Award in 2018.

Lukas Piotrowsky (Graduate Student Member, IEEE) was born in Neuwied, Germany, in 1990. He received the B.Sc. degree from the University of Applied Sciences Koblenz, Koblenz, Germany, in 2016, and the M.Sc. degree in electrical and information engineering from Ruhr University Bochum, Bochum, Germany, in 2018.

Since 2018, he has been a Research Assistant with the Institute of Integrated Systems. His research interests include millimeter-wave radar system design and embedded signal processing.